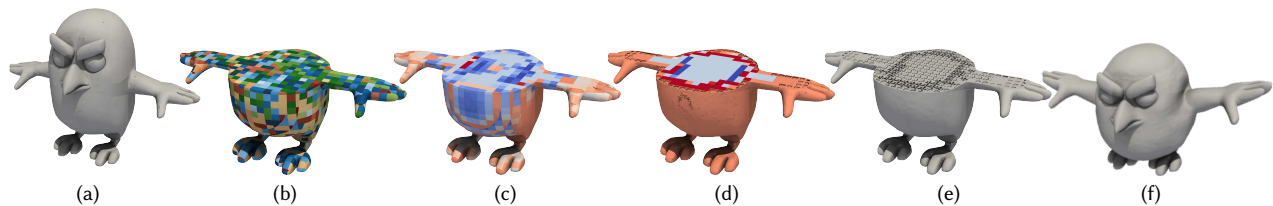


# Cut-Cell Microstructures for Two-scale Structural Optimization

Davi Colli Tozoni<sup>1,2</sup> , Zizhou Huang<sup>1</sup> , Daniele Panozzo<sup>1</sup> , and Denis Zorin<sup>1</sup> 

<sup>1</sup> New York University, New York, US

<sup>2</sup> nTop, New York, US



**Figure 1:** (a) Our method starts with an arbitrary initial surface mesh. (b) We intersect the object with a regular grid partitioning it into interior cubic cells and boundary cut cells (c) We perform optimization for a particular deformation behavior (wings going up by a prescribed distance with pressure on the top) and obtain a material distribution (Young’s modulus is shown in color) for all cells (d) Each boundary cut cell is replaced by a cell microstructure from our novel family to match Young’s modulus computed by the optimization in (c), and then a second optimization is performed on interior cells to compensate for the difference between the effective and optimized Young modulus (e) Finally, the interior cells are replaced with cubic-cell microstructures with effective material properties equivalent to these computed by the second optimization (f) The deformation result on the final model closely matches the prescribed target deformation.

## Abstract

Two-scale topology optimization, combined with the design of microstructure families with a broad range of effective material parameters, is widely used in many fabrication applications to achieve a target deformation behavior for a variety of objects. The main idea of this approach is to optimize the distribution of material properties in the object partitioned into relatively coarse cells, and then replace each cell with microstructure geometry that mimics these material properties. In this paper, we focus on adapting this approach to complex shapes in situations when preserving the shape’s surface is essential.

Our approach extends any regular (i.e. defined on a regular lattice grid) microstructure family to complex shapes, by enriching it with tiles adapted to the geometry of the cut-cell. We propose a fully automated and robust pipeline based on this approach, and we show that the performance of the regular microstructure family is only minimally affected by our extension while allowing its use on 2D and 3D shapes of high complexity.

## CCS Concepts

• **Computing methodologies** → **Shape modeling**;

## 1. Introduction

Additive manufacturing enables easy fabrication of complex geometric structures designed with specific effective material properties in mind, with a broad range of applications from lightweight but strong structures in aerospace to shoe soles, prosthetic devices, and flexible robot parts [nTo23; Car23]. While the more complex geometry can be easily handled by modern 3D printing software and hardware, optimized design of such objects is a fast-growing research area. Most traditional engineering analysis and optimization software is not suitable for this task, due to limitations on the complexity and scale of geometry that can be handled.

A popular approach is to directly optimize the shape of the entire structure by using topology optimization and/or shape optimization. However, the computation cost of these direct methods is high, especially for large objects, often requiring HPC clusters [AALS17]. An alternative is to use a two-scale approach: (1) a material optimization is performed on a voxelized grid to compute material properties varying between voxels and resulting in desired target deformation behavior, and (2) each voxel is replaced by a geometrical structure (microstructure tile) with effective properties matching the computed solid material properties in the voxel. The advantage of this strategy, compared to whole object high-resolution topology optimization, is that step (1) can be very efficient and step (2) can be

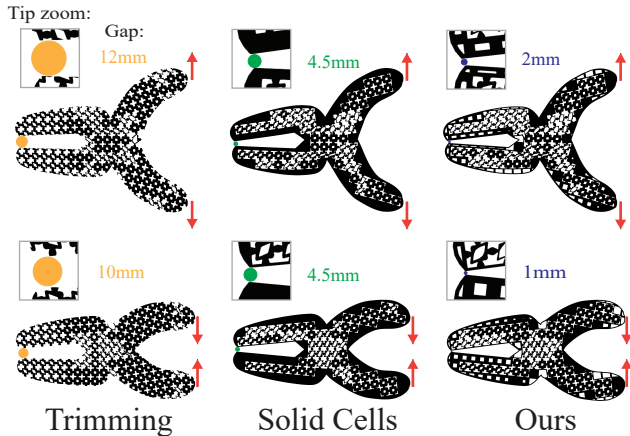


**Figure 2:** Two examples comparing simpler baselines, trimming (left) and solid cells (middle), with our approach (right). The scissor is optimized to close when the handles are pulled apart (top row) or pulled together (bottom row). Our approach succeeds in both cases, while trimming performs very poorly, and solid cells are somewhere in between. Numerically, when comparing actual displacements against target displacements, there is a clear advantage for our method. For the example in the top row, the error is 0.0929 / 0.0612 / 0.0495 for trimming / solid cells / our method. For the example in the bottom row, the error is 0.0634 / 0.0293 / 0.0140 for trimming / solid cells / our method. The error is computed using the 1st term of Equation 4 normalized by target boundary length. We provide a detailed comparison against the solid cells baseline in Section 4.

reduced to a lookup table: a family of microstructure tiles, mapping material properties to geometry, which can be precomputed using a cluster, and then used for multiple designs.

Unavoidably, the voxelization of a shape leads to artifacts in the boundary, becoming problematic in applications where the shape’s boundary matters, which is common in many settings, from moving engine parts to prosthetic devices. Trivial approaches, such as trimming the microstructure to follow the boundary or filling the voxels on the shape’s boundary, lead to a major change in effective microstructure properties in these cells and significant deviations from the intended behavior under loads (see Figure 2 and 3 for a comparison and Section 4 for a detailed analysis). To address this problem, these approaches have been extended, in 2D only, from regular grids to boundary-aligned structured meshes [TDJ\*20]. Still, the strong requirement for mesh uniformity and quality makes them less robust than the grid-aligned methods, which are still the standard de facto in industry [nTo23]. In 3D, such an extension is much more difficult: while planar quad mesh generation is possible (although quads may be far from parallelograms required by [TDJ\*20]), generating boundary-aligned hex meshes is still an open problem, with a recent state-of-the-art method yielding a 50% success rate on a recent benchmark [LB23].

We propose a novel family of cut-cell microstructures to extend existing 2D or 3D regular tiling microstructure families to shapes with a complex boundary. Our construction ensures that the shape boundary exactly matches the input (with the exception of tunnels needed to remove the internal material after printing, Figure 12),

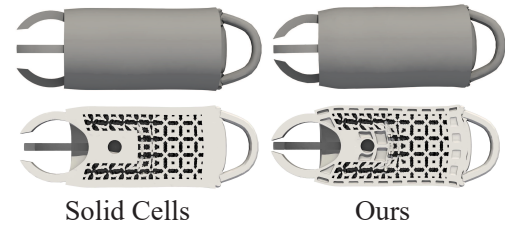


**Figure 3:** Comparison between the solid baseline (left) and our method (right) in 3D. The top row shows both versions seen from the outside (as someone using the gripper would see it), while the bottom row shows section cuts of both shapes. The structure is optimized so that its jaws close together under a compression force on the handle (gripper’s right side). The baseline example fails to reach the prescribed deformation.

and, in combination with an interior structure, leads to accurate matching of the prescribed deformation behavior. Our algorithm is the first method enabling two-scale shape optimization on very complex shapes in 3D, in a fully automated and robust way, with the resulting complex geometric structures including the input boundary precisely.

We demonstrate its effectiveness by combining our cut-cell family with a variant of the microstructure family proposed in [TDJ\*20] to realize complex 3D shapes with controllable material properties, and evaluate their properties by fabricating them using 3D printing and testing them in a set of controlled load experiments.

To summarize, the contributions of this paper are:

- An extended microstructure construction that includes a structure for boundary cells which ensures their connection to the interior cells and supports arbitrary surface geometry.
- A novel two-stage algorithm of two-scale structural optimization, optimizing the material properties for both interior and boundary cells.
- A mapping from material to shape parameters of the boundary microstructure, in two and three dimensions.
- A robust geometric pipeline for constructing microstructure in-fill for arbitrary input shapes with surface preservation, not considered in previous work.
- Quantitative and qualitative physical evaluation of the optimized structures.

## 2. Related Work

**Microstructure design and optimization.** There is extensive literature on the design of elastic and other types of metamaterials/microstructures. We refer to the books, e.g., [CD99; Mil02; Tor02] for the foundational work and the recent survey [KMvHW19] for more up-to-date references. The approaches to the design of periodic microstructures with prescribed homogenized properties rely on topology optimization, going back to [Ben89; BS03], and shape optimization, as well as combinations of the two. Examples in computer graphics literature include [SBR\*15] (topology optimization) and [PZM\*15] for shape optimization, with many more in studies in material science and engineering. These works, as well as, e.g.,

[ZSCM17], consider constructing families spanning a broad range of elastic properties, with the potential maximally achievable ranges characterized in [MBH17].

**Global topology optimization.** In [WDW16; AALS17; LHZ\*18], topology optimization was scaled up to high-resolution uniform and adaptive 3D grids. [WAWS18] performs high-resolution topology optimization with additional constraints to create an evenly distributed porous small-scale structure minimizing compliance for specific loading scenarios. Even with these improvements, direct topology optimization at the microstructure level remains computationally expensive: e.g., a modest cell resolution of  $32^3$  combined with an equally modest  $32^3$  resolution at the coarse level requires over 1 billion cells to work with. To avoid these high computational costs, we favor a two-scale optimization approach.

**Two-scale optimization using microstructures.** Two-scale optimization uses microstructures to optimize the deformation behavior of objects efficiently by separating the problem into two scales through the partitioning of an object into cells. Fine-scale structures for individual cells are often precomputed to yield a particular range of effective material properties within the limit of infinitely fine cells. The coarse-scale optimization is performed by treating the whole cells as made of homogeneous material. Some works, e.g., [LLWW18], do not precompute microstructures and optimize at both macro- and microscale simultaneously. This approach, while most flexible, is computationally very expensive and does not support well typical workflows. Recent surveys [WSG21] and [PP19] provide an overview of the approaches and recent work in this domain.

All two-scale optimization approaches rely on tiling the input shapes with microstructures. The most common approach, and the current standard de facto in industry, is voxelization. Papers using voxelization focus on rectangular structures, as examples [PZM\*15; ZSCM17]. Other works [RWH22; XB15; DBHG21] approximate arbitrary shapes with collections of cubes. This approach is unsuitable for applications that require preserving the shape of the surface (e.g., a wheel would not roll) or its appearance. This problem is exacerbated for relatively coarse grids of cells, which are often unavoidable due to limitations in the minimal beam thickness in many 3D printing technologies: an exception is [SPP21], where an expensive and slow printing process is used to reduce the size of voxels. Yet, despite the high resolution, the resulting surfaces are still not smooth.

The conforming tiling construction is introduced in [TDJ\*20] for 2D and [WCOR21] for 3D, where a voxelization is replaced by a boundary adapted, isotropic, low distortion quad or hexahedral tiling, and the domain of the microstructure families is extended accordingly. In addition to the increased complexity in the family design, the main drawback of these methods is that structured meshes with these properties are challenging to generate for arbitrary geometries. While some solutions exist for 2D [TDJ\*20], the solution to conforming hexahedral mesh generation in 3D is a challenging open problem [BRK\*22], where the failure rate of state-of-the-art methods is shown to be around 50%. Finally, the approach [GWS19; GS17; GPZ19] for 2D and surface structures can be viewed as a partial conforming tiling construction: it uses a simple rectangular

microstructure with two parameters, and a frame field to define the directions and scale for cells from a simple family. The frame field orientations and other fields are chosen by optimization. Similarly to the previous category, this approach is also difficult to generalize reliably to 3D volumes due to a more complex structure of 3D fields [PCS\*22].

Our approach shares the benefits of conforming tiling constructions, as it allows the reproduction of boundaries for complex geometries, but is doing so by extending the voxelization methods using a cut-cell approach. Our algorithm combines the robustness and simplicity of the voxelization methods with the advantages of conforming tiling constructions without requiring a difficult-to-build quad or hexahedral mesh.

**Special Shape-Adapted Microstructures.** [KPCP18] uses a special type of 2D triangular auxetic structure to effect conformal surface deformations. This method requires domain meshing with triangles close to regular. Similarly, a recent paper [MPI\*18] uses 2D spiral microstructures. As an alternative to periodic microstructures, [MDL16; MSDL17] construct randomized printable structures with control over Young's moduli both for isotropic and anisotropic target properties. However, it cannot independently control the Poisson's ratio, and the behavior of randomized structures is less controllable overall.

**Variable Base Material.** Our focus is fabrication methods supporting single base material due to their wide availability, lower cost, and support for stiff materials (metal). Having access to controllable base material further widens the range covered by microstructures: [BBO\*10] designs and fabricates objects satisfying an input deformation using actual material properties variation, with fabrication done using a multi-material printer. [STC\*13] applies discrete material optimization to achieve desired deformations of complex characters, also using multi-material printing for fabrication.

### 3. Method

#### 3.1. Material Optimization Primer

We provide a short introduction to material optimization and two-scale optimization using microstructures to keep the paper self-contained. We refer to [PZM\*15; SBR\*15] for more details.

Let  $\Omega$  be the domain of a solid. Loads (Neumann boundary conditions) and/or Dirichlet boundary conditions are applied on some parts of  $\Omega$ , typically on the boundary. The deformed state is obtained by solving the linearized elasticity equation for the displacement  $u$ ,

$$-\nabla \cdot [C : \varepsilon(\mathbf{u})] = 0 \quad \text{in } \Omega, \quad (1)$$

where  $C_{ijkl}$  represents the 4th order elasticity tensor and  $\varepsilon(\mathbf{u}) := \frac{1}{2}(\nabla \mathbf{u} + (\nabla \mathbf{u})^T)$  is the linearized Cauchy strain tensor of the averaged deformation. The notation  $A : B$  is used to denote the contraction  $\sum_{k,l} A_{ijkl} B_{kl}$ . The boundary conditions have the form  $\mathbf{u}|_{\partial\Omega_D} = \mathbf{u}_0$ , where  $\mathbf{u}_0$  are prescribed boundary displacements on the part of the boundary  $\partial\Omega_D$  and  $C : \varepsilon(\mathbf{u})|_{\partial\Omega_N} = \mathbf{f}_0$ , where  $\mathbf{f}_0$  are external forces applied to the part of the surface  $\Omega_N$ .

Our goal is to minimize a function  $\mathcal{E}$  of the displacement  $u$ . For example, to obtain a desired deformation of a part of the object's

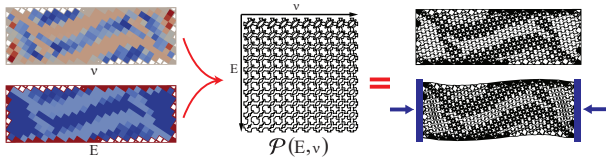


**Figure 4:** Two-scale optimization pipeline. (left) we run material optimization on a bar with square cells; (middle) a map  $\mathcal{P}$  is used to map material properties to geometry; and (right) we obtain the final shape, which deforms as expected.

boundary under a certain load condition (Figure 1),  $\mathcal{E}$  is the  $L_2$  norm of the difference between  $u$  and the target deformation. We do this by changing the spatially varying material properties (Young's modulus and Poisson ratio) encoded in the spatially varying tensor  $C$ . The problem is constrained by the linearized elasticity PDE:

$$\min_C \mathcal{E}(\mathbf{u}, C), \text{ subject to (1)}. \quad (2)$$

This problem is closely related to widely used topology optimization formulations [BS03]. Additional constraints are usually added to this problem to force, in every point in space, either homogeneous material properties or zero density, thus obtaining an object with homogeneous material properties and possibly holes. These constraints make this large optimization problem even harder to solve.

**The two-scale approach.** A two-scale optimization approach [PZM\*15; TDJ\*20] uses a microstructure family  $\mathcal{P}$  to make solving this problem orders of magnitude cheaper.  $\mathcal{P}$  is a map from an elasticity tensor  $C$  (or equivalently material properties such as Young's modulus and Poisson's ratio) to a periodic geometric pattern with the same homogenized stiffness tensor (see Figure 4). The periodic patterns are typically characterized by a set of shape parameters. Equipped with  $\mathcal{P}$ , the two-scale optimization solves the problem in two steps. First, a material optimization problem, in which the per-voxel value of the stiffness tensor is optimized, is solved on a voxel grid at a coarse scale:

$$\min_{C \in D} \mathcal{E}(\mathbf{u}, C), \text{ subject to (1)}, \quad (3)$$

where  $D$  is the domain of the map  $\mathcal{P}$ , which is a subset of all stiffness tensors that can be realized by using a family of cell microstructures. After solving this small problem (e.g., this problem has around 500 degrees of freedom for the 2D examples in Figure 16 and can be solved within seconds), the map  $\mathcal{P}$  is used to replace the cell with the corresponding microstructure geometry; the resulting object with complex geometric structure can be fabricated using a single material.

The two-scale approach described above has two important challenges: (1) designing the microstructure family  $\mathcal{P}$  and (2) reducing the error introduced in the object's shape due to a coarse voxel grid, as fabrication constraints typically do not allow one to make the voxels too small. Our focus in this paper is on the latter problem, which has received little attention in the literature. For (1), we borrow and slightly modify the family proposed in [TDJ\*20], as detailed in Section 3.5.

## 3.2. Overview

We describe our approach to computing an infill structure producing desired deformation behavior for an object for 3D, but the same construction works for 2D: we highlight the required modifications in Section 3.8. In Section 4, we demonstrate how these steps contribute to the quality of the results. The approach is composed of five steps:

1. **Cell Partition.** We produce a cell partition of the domain  $\Omega$  by intersecting it with a regular grid; the partition consists of cubic (square, in 2D) cells in the interior and cut cells, obtained by intersecting a cubic cell with the interior of the object. Each cell is partitioned into tetrahedra, with the same material property variable  $C_i$  assigned to all tetrahedra corresponding to a cell.
2. **Initial Material Optimization.** We solve the problem defined in Equation 2, with constant properties per cell, computing material parameters  $C_i$  by minimizing the objective  $\mathcal{E}$  (see Equation 4), with material parameter bounds for the interior cells determined by the domain of  $\mathcal{P}$ , and for boundary cells inferred from cell geometry. For interior cells,  $(E, \nu)$  are used as material parameters. For boundary cells,  $E$  is the only optimized material parameter and we keep  $\nu$  fixed at the base material value.
3. **Generation of Cut-Cell Geometry.** For the boundary cells, we use a one-parametric family of microstructures, with a single parameter for each cell, the interior void size. We determine this parameter for each boundary cell so that the effective material properties approximately match the target material and compute the cell geometry for this void size (Section 3.5).
4. **Interior Material Refinement.** We build a hybrid geometry using solid interior cells with variable material  $C_i$  assigned to each interior cell but the actual microstructure geometry from Step 2 for the boundary cells. For this new volumetric mesh, with the complex structure on the boundary only, we repeat the material optimization for interior cells, but, this time, with material properties fixed to the base material for already inserted boundary cell geometry and variable material properties for the internal cells (Section 3.6).
5. **Surface Extraction.** The geometry of the boundary cells is merged with the microstructure geometry produced from optimized material properties from the previous step via the map  $\mathcal{P}$ . Optionally, we add tunnels to the exterior to allow fabrication using 3D printing methods requiring residual material removal (Section 3.7).

We summarize the main steps of our algorithm in Figure 5.

### 3.3. Step 1. Cell Partition

The input for this step is a surface mesh and a background regular grid, with each grid cell corresponding to a microstructure tile in the final structure. The output is a tetrahedral mesh of the interior of the surface mesh, with the regular grid cells split into tetrahedra. This mesh is used for the first material optimization.

This problem could be solved by computing a 3D arrangement [HK22] or by cut-cell meshing tools [TBFL19; ABM98], followed by postprocessing to tessellate the interior of each cell with tetrahedra while ensuring a conforming mesh at the cell boundaries.

As shown in Figure 6, we opted for a more direct and robust

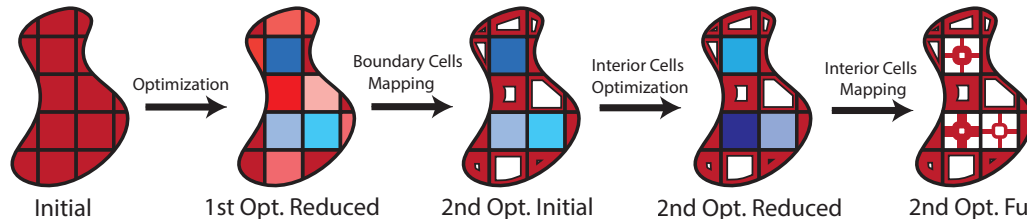


**Figure 5:** Summary of our method, showing the main steps of our algorithm. Quantitative results of each step are shown in Table 1. Dark red represents our base material. Different tones of red represent variable material on the boundary, while tones of blue are used for material properties of interior cells. "Reduced" refers to the mesh used in the optimization (either solid interior cells or solid boundary cells), and "Full" refers to the final mesh with microstructure geometry that can be used for fabrication.

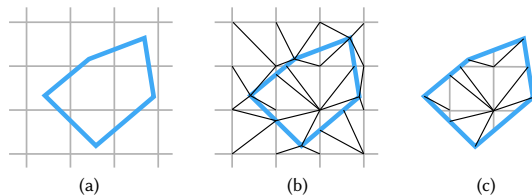


**Figure 6:** Illustration of cell partition. (a) Initial surface mesh with a background regular grid. (b) Triangular/Tetrahedral mesh of the bounding box. (c) Final mesh after removing triangles/tetrahedra outside of the surface mesh.

solution, creating a tetrahedral mesh with fTetWild [HSW\*20], while providing both the surface mesh and grid faces as input. The fTetWild tool outputs a tetrahedral mesh of the bounding box of the input mesh. We then filter the tetrahedra outside the object surface using the winding number [JKS13], and assign the resulting tetrahedra to the cell of the grid containing its barycenter. Eventually, we obtain a tetrahedral mesh of the surface, while each tetrahedron is inside a grid cell. We use a geometrical tolerance of  $10^{-3}$  for fTetWild. This approach is insensitive to surface mesh imperfections and simultaneously allows us to maintain the high mesh quality needed for simulation. fTetwild guarantees that the tetrahedra are of good quality as long as the mesh optimization converges. We do not observe failure in the meshing process of our examples.

To satisfy the minimum thickness requirement in 3D printing, the maximum size of the internal voids of boundary cells is restricted. However, some boundary cells might be too thin even without internal voids. If a thin boundary cell is adjacent to an interior cell, after the interior cell is replaced by the microstructure, this boundary cell may violate the minimum thickness. To avoid this, we change the type of some interior cells into boundary cells, although they are not cut by the boundary surface. Specifically, we compute the distance between the surface cutting a boundary cell and its internal boundary faces, edges, and vertices, shared with other internal cells; if the distance is too small, we transform all internal cells sharing this element into a boundary cell. See Figure 7 for an example.

### 3.4. Step 2. Initial Material Optimization

We solve problem (3) with the following functional:

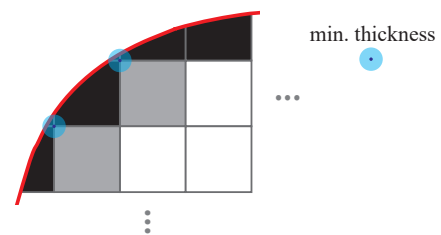


**Figure 7:** Interior Cells that are too close to the boundary may cause thin features in the shape. To avoid issues during printing and non-smoothness in displacement behavior, we consider those as boundary cells. The drawing shows boundary cells (in black) touching the (red) boundary and two quad cells (in dark gray) that are too close to the boundary, according to a min. thickness parameter.

$$\mathcal{E}(\mathbf{u}, C) = \int_{\partial\Omega^t} (\mathbf{u}(C) - \mathbf{u}^t)^2 dA + w \int_{\Omega} \|\nabla C\|^2 dA, \quad (4)$$

where  $\partial\Omega^t$  is typically a part of the boundary of our domain for which we prescribe target displacements  $\mathbf{u}^t$ ,  $w$  is a weight to adjust the smoothness of the material distribution. The constraints on the problem consist of a set of linear bounds for the domain of material properties. For interior cells, we constraint the material properties ( $E, \nu$ ), i.e. Young's modulus and Poisson's ratio, to be inside the domain of  $\mathcal{P}$ , shown in Figure 8. For boundary cells, we add constraints on Young's modulus, preventing the creation of features smaller than a predefined thickness.

As seen in Equation 4, our objective has two terms. The first corresponds to the deformation error, which measures the difference between the simulated displacement  $\mathbf{u}(C)$  and the target  $\mathbf{u}^t$ . The second term is a regularization term, aiming to achieve a smoother spatial material variation, which helps to reduce large differences in microstructure geometry when transitioning between neighboring cells, which may lead to local deformation artifacts.

The problem is discretized using the finite element method [SDG\*19], and the adjoint method is used to compute the gradient of the target functional with respect to elasticity parameters [HTG\*22]. The optimization itself is performed using L-BFGS with box constraints.

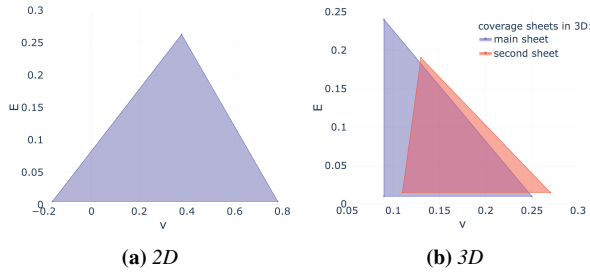


**Figure 8:** Coverage of material parameter properties in the families we use. Our coverage regions are approximated to triangles, so they can be easily added as constraints in our optimization.

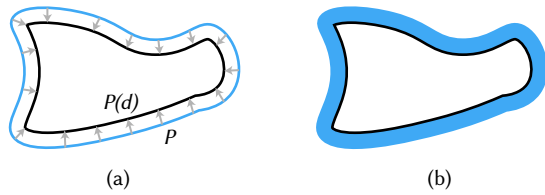


**Figure 9:** Illustration of creating a cavity to reach a certain volume ratio based on the surface offset. (a) The surface  $P$  is offset by  $d$  to get  $P(d)$ . (b) Volume inside  $P(d)$  is dropped to match target volume ratio  $r$ .

### 3.5. Step 3. Generation of Cut-Cell Microstructure

While we can use  $\mathcal{P}$  to find microgeometry for the internal cells, the construction of the map from material properties to geometry is based on periodic-material homogenization and requires cells to be cubes: in this step, we provide a construction of a microstructure family for boundary cut cells with arbitrary geometry.

Our approach is to create a 1D bijective smooth map  $\mathcal{P}_b$  between volume fraction  $r$  of the filled part of a cell and Young's modulus  $E$ , using the fact that there is usually a strong connection between stiffness and solid material volume fraction (see paragraph below detailing our mapping) in simple cell geometries with a single void, while the shape of the void has less impact. We can obtain such single-void one-parametric families for arbitrary cell shapes by defining our microstructure geometry to be solid between the polygonal boundary  $P$  of the cell and an offset  $P(d)$  of  $P$  (Figure 9), where  $d \geq d_{\min}$  is a parameter interpolating between the minimal wall thickness ( $d_{\min}$ ) and a fully filled cell. We construct  $P(d)$  for an arbitrary cell shape using a signed distance function (SDF). The cell boundary mesh  $P$  is converted to an SDF (we use OpenVDB [Mus13]), and then we call the **offset** function in OpenVDB, and finally convert the offset SDF back to a mesh. Figure 10 shows three examples of boundary cell geometry in real models. Notice that, in 3D, we may need to add additional openings to avoid enclosed voids, as discussed in Section 3.7.

Next, we determine the correspondence between volume fraction  $r$  and the offset  $d$  for a specific cut cell geometry. Denote the volume enclosed by surface  $P$  as  $V$ , and the volume enclosed by surface  $P(d)$  as  $V(d)$ . Given a fixed  $r$ , our goal is to find the offset value  $d$  so that

$$V(d) = (1 - r)V.$$

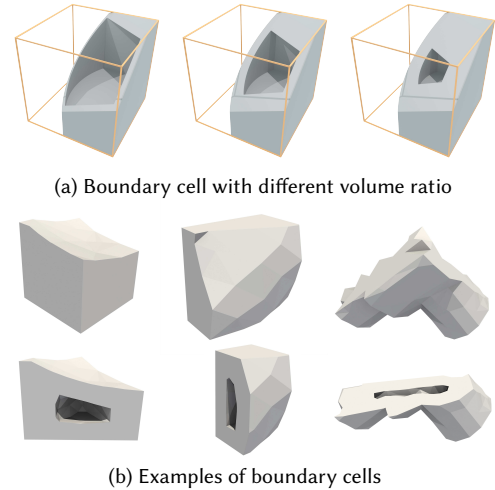


**Figure 10:** Boundary cell geometry in 3D. (a) The cross-section of a cut-cell enclosed by the grid partition is in yellow. (b) The bottom row shows the cross-section of the top row.

This is a 1D root-finding problem for a monotonically increasing function, so we use a binary search to find the root  $d$  with a relative tolerance of 0.01.

**From Material Properties to Volume Fraction.** The relationship between the effective Young's modulus and volume ratio, in general, depends on the shape of the cell and, in the case of non-tileable cells, may even be difficult to define precisely, as it is unclear how to perform correct homogenization in this case (homogenization requires periodic tiling). However, a rough approximation of this dependence can be obtained from a one-parametric family of complete cubic cells, which can be tiled periodically. In this case, we can compute the effective Young's modulus by averaging Young's modulus on orthogonal directions  $(x, y, z)$  (obtained from the homogenized elasticity tensor), for a variety of interior void shapes, to verify that the dependence on the shape of the void is not strong (Figure 11). As a result, we have a function  $E(r)$  which we invert to map the optimized Young modulus values  $C_i$  (obtained at Step 2 for boundary cells) to the volume ratios  $r$ . For a specific choice of cell boundary, we determine the offset  $d$  from  $r$  as described above, building a complete map from  $C_i$  to a boundary cell microstructure. While considering only full cells (for which homogenized parameters can be obtained) provides a limited validation of the approach, this heuristics is further validated by the observed improvement in the optimized result behavior demonstrated in Section 4.

The need for precise knowledge of the effective material properties of a cell is made less critical for this stage by the next step, which compensates for the errors introduced in the boundary cells.

### 3.6. Step 4. Interior Material Refinement

Given a target volume ratio for each boundary cell determined by their target Young modulus computed in Step 1, we determine the offset for the cell microstructure in Step 3. We perform the offsets for all boundary cells in parallel, append the offset surface mesh to

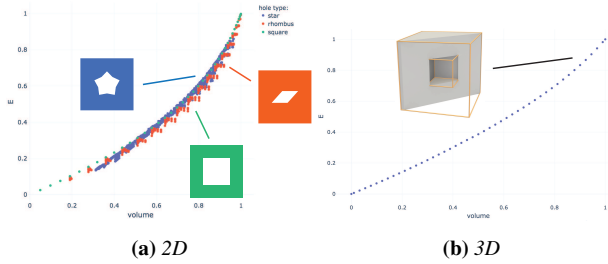


**Figure 11:** Volume ratio to average Young's modulus map. The left figure represents the map for 2D microstructures, where each color represents a different shape of the opening, while the figure on the right represents the map in 3D.

the original mesh, and then create a new volumetric mesh with the approach used in Step 2.

Replacing the boundary cells with their new offset geometry introduces a small, but measurable, increase in the objective function: To further increase the accuracy of the solution and compensate for this increase, we run a second round of material optimization fixing the geometry and material properties of the boundary cells, and optimizing only the regular, interior cells.

On the new mesh, which has explicitly meshed cut-cell microstructures on the boundary and regular grid cells in the interior, we solve a material optimization problem with fixed base material in boundary cells (as their microstructure is already integrated into mesh geometry). While the overall complexity of the optimization increases, as the simulation needs to be done on a finer mesh in boundary cells, it is still much lower than the complexity of direct microstructure shape or topology optimization, as the number of optimization variables is lower. While this optimization always reduces the objective value, its effect varies depending on the example (Table 1). In principle, the process can be iterated, by switching boundary and interior cell optimization, but using explicit geometry for interior cells is expensive, and little additional benefit can be expected.

### 3.7. Step 5. Surface Extraction

To extract the surface from the implicit volumetric functions (see Section 3.9) of the internal and boundary cells, we first compute the union of all interior cell SDFs and intersect it with the SDF obtained in Step 5 which included boundary cell geometry only. The surface mesh is extracted from the resulting SDF using the marching cubes method. We use a resolution of  $50 \times 50 \times 50$  per cell for the SDF (note that this effective resolution is used in a sparse volumetric representation in OpenVDB).

By construction, our boundary cells have a solid layer covering the model surface, which will prevent uncured resin or unmelted powder from being removed after fabricating the model. To make the model fabricable, we add tunnels to each boundary cell (Figure 12). The tunnels defined below will be a boolean union of spheres and cylinders with a uniform radius  $r$ . We first go over boundary cells with internal voids and consider the parts  $B_E$  of their surfaces that belong to the outer surface. We denote the barycenter of the internal void in each cell as  $P_E$ . Although the internal void is not necessarily

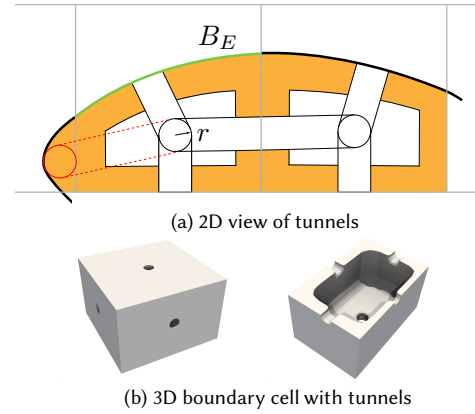


**Figure 12:** Tunnels connecting boundary cells. (a) The gray lines represent the grid partition,  $B_E$  for one boundary cell is shown in green, the tunnels are cylinders with radius  $r$ , and solid parts are shown in yellow. The red circle is too large to fit into the boundary cell, so we fill the cell completely. (b) A boundary cell with internal void and tunnels (left) and its cross-section (right).

connected when the boundary cell is not convex, it did not happen in our examples. In the case where there are multiple internal voids in one boundary cell, one can pick  $P_E$  to be the barycenter of one of the internal voids. If the sphere centered at  $P_E$  with a radius  $r$  intersects  $B_E$ , constructing a tunnel to the exterior may break the cell and its surface into pieces, in this case we completely fill this cell. Otherwise, if the sphere centered at  $P_E$  with a radius  $r$  is completely inside the boundary cell, we include the sphere as part of the tunnels. After the spheres are created, we connect the  $P_E$  of every two adjacent spheres (we call two spheres are adjacent if the corresponding boundary cells share at least one face) by a cylinder with radius  $r$ , and these segments form a graph consisting of disjoint connected components. For each such connected component, we create a cylindrical tunnel from one void center to the object's surface. To remove the materials inside interior cells, at least two tunnels are created from internal cells to adjacent boundary cells with voids. To avoid the decrease in volume caused by creating tunnels, we pick the smallest possible radius as long as the 3D printing materials can be removed.

### 3.8. 2D Algorithm

Our 2D pipeline closely follows the 3D pipeline, using the Triangle library [She96] instead of fTetWild, and using our own implementation of marching squares as OpenVDB does not support 2D domains. An advantage of the Triangle is that it allows us to represent the boundaries exactly, without introducing a geometric approximation error. Tunnels are not added to the 2D boundary cells as they are not necessary for fabrication.

### 3.9. Construction of $\mathcal{P}$

We use the method introduced in [TDJ\*20; PZM\*15] for creating microstructure families for the interior cells both in 2D and 3D. However, we do not use their rhombic shape parameter, as in our

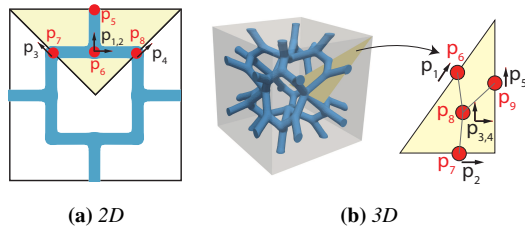


**Figure 13:** Cell parameters for 2D and 3D, interior cells.

case we will use only square/cubic cells. We briefly review this construction here.

First, a homogenization map  $H(\mathbf{p})$  is obtained for a low-parametric family of microstructures, with parameters  $p_i$  shown in Figure 13, consisting of graph vertex positions and radii at these vertices determining how thick the microstructure is at this location. The method of [PRZ17] is used to construct the implicit curve/surface bounding the microstructure geometry from the graph and radii.

The 3D microstructure has cubic symmetry [PZM\*15] by construction, which means Young's modulus and Poisson's ratios are the same in every axis-aligned direction, and there are only 3 independent parameters in the tensor, Young's modulus  $E$ , Poisson's ratio  $\nu$  and the shear modulus  $G$ . We run a sweep of the parameter values in a given range  $[p_i^{min}, p_i^{max}]$  for each parameter  $p_i$ . Consider  $B_p$  the  $n$ -dimensional box of admissible parameter values. Each combination of values is used to generate a microstructure cell geometry using the implicit surface definition of [PRZ17]. The value of  $H(\mathbf{p})$  is obtained as the effective value of the elasticity tensor parameters, so the function  $H(\mathbf{p})$  maps  $\mathbf{p}$  into  $\mathbb{R}^3$ .

The map  $H(\mathbf{p})$  is not bijective as it typically maps a higher-dimensional space into a lower-dimensional space. In [TDJ\*20], a sequence of dimension reductions is used to identify a subspace  $D$  in the space of shape parameters equal to the dimension of the elasticity material parameter space (3 in our case). The map  $H(\mathbf{p})$  restricted to this subspace may still be not bijective, but its image  $H(B_p)$  can be partitioned into parts on which it is invertible; specifically, we construct simplices in the subspace of shape parameters and split  $B_p \cap D$  into connected subdomains  $D_j$  by simplex orientation. On each of  $D_j$ , we can invert  $H(\mathbf{p})$ . We further restrict it to the two-dimensional space of isotropic material parameters parameterized by  $(E, \nu)$  to obtain the material-to-geometry map  $\mathcal{P}_i(E, \nu) : H(D_i) \rightarrow B^p$ . Figure 8 presents the coverage regions for our 2D and 3D families. Notice that for 3D we have two different material coverage sheets, with the blue one covering most of the space and being chosen as our main material range.

Following [PZM\*15], our microstructures are constrained to have cube symmetries, which are guaranteed to have the same Young's moduli and Poisson's ratios in every axis-aligned direction. To evaluate the approximation error and anisotropy of our interior microstructure family  $\mathcal{P}$ , we uniformly sample on the triangle domain in Figure 8(b), compute the absolute error between the target and real homogenized material properties, and the isotropy measure of the microstructures. We adopt the same isotropy measure from

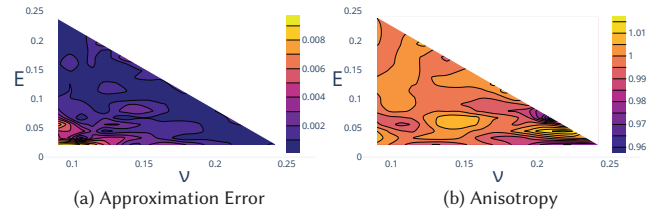


**Figure 14:** Approximation error and anisotropy distribution of our 3D microstructure family.

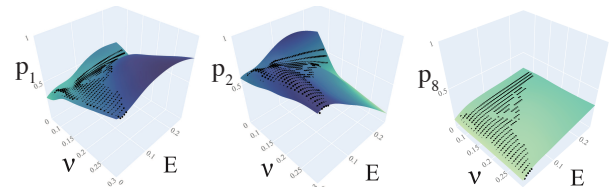


**Figure 15:** Examples of shape parameter dependence on materials in our 3D family. These maps correspond to our main coverage sheet.

[PZM\*15]:

$$A = 2(1 + \nu)G/E.$$

Besides, we also measure the approximation error

$$e = |E - E_{\text{trg}}| + |\nu - \nu_{\text{trg}}|,$$

where  $E_{\text{trg}}$ ,  $\nu_{\text{trg}}$  are the target elastic parameters. As shown in Figure 14, the approximation error is below 1% and the anisotropy is within 4%.

Figure 15 shows examples on the final map from material properties  $(\nu$  and  $E$ ) to geometric parameters  $p_i$ .

#### 4. Evaluation

Our algorithm is implemented in C++ and uses Eigen [GJ\*10] for the linear algebra routines, PolyFEM [SDG\*19] for finite element simulation in 3D and MeshFEM [PZM\*15] in 2D, fTetwild [HSW\*20] and triangle [She05] for meshing, and Pardiso [ABB\*20; BSJ\*20; BESS19] for solving linear systems. We run our experiments on a cluster node with an Intel Cascade Lake Platinum 8268 processor limited to 32 threads.

We demonstrate on a range of 2D (Section 4.1) and 3D (Section 4.2) examples that our method is the first that can reliably and automatically create both 2D and 3D objects closely matching the prescribed deformations while preserving the object boundary. We also compare our results with alternative methods (Section 4.3), including baselines with trimmed and solid cells, where our approach consistently outperforms the baselines, and a more technically involved method applicable only to 2D, where our results are of comparable quality.

##### 4.1. 2D examples

We experimented with six 2D models shown in Figure 16. Visually, our results closely match the specified target, both in direct



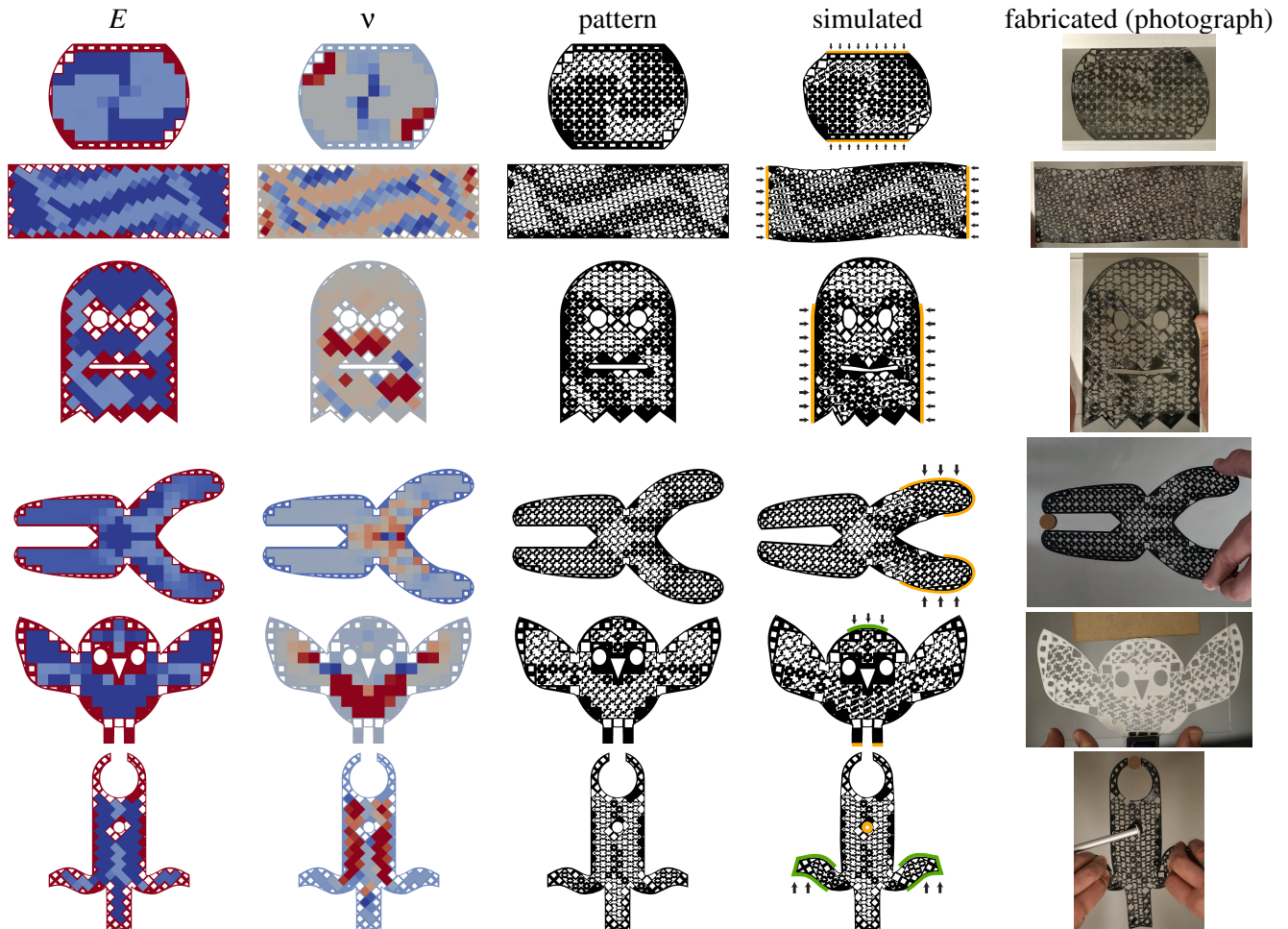


**Figure 16:** A gallery of 2D examples. From left to right: optimized material distribution (Young's modulus and Poisson's ratio), final geometry at rest, deformed geometry (simulated), and photographs of deformed pattern (fabricated). In the simulation column, surfaces with Dirichlet and Neumann boundary conditions are marked in orange and green respectively, with the displacement and force directions in black arrows.

simulation (done on a dense mesh of the final geometry) and in our physical validations. For physical validation, we fabricated the models using FDM printing with a TPU 95A filament on a Prusa i3 MK3S and an Ultimaker 3 (see Figures 17 and 18). Numerical results, breaking down the effect of the different optimization stages, are available in Table 1 and discussed in more detail in Section 4.3.

In Figure 16, the examples from top to bottom are: **Disk**. The objective is to obtain a shear-like deformation, bulging on the top left and bottom right, whenever the disk is compressed in the vertical direction. **Sine bar**. The bar is optimized to match a sine wave shape under compression in the horizontal direction. **Happy Ghost**. The Pacman ghost shape is optimized to smile when compressed on the sides. We add target displacements such that the middle region (of both the top and bottom) of the mouth displace down. **Pliers**. The plier is optimized to close when the handles are pulled together. **Bird**. The shape is optimized to flap its wings whenever its head is pushed down. In this case, we add a Dirichlet boundary condition on the bird's feet to keep it in place. **Sword Gripper**. The gripper has a rounded hole in the middle that is used to hold the shape in

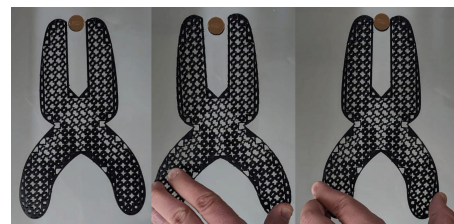


**Figure 17:** Fabricated pliers (black TPU). Rest shape on the left; moving the handles apart in the middle; compressing the handles to hold the object on the right.

place and should not deform during the operation. The mechanism closes whenever the handle moves up.

Additionally, we show two deformation sequences for the plier (Figure 17) and sword gripper (Figure 18).

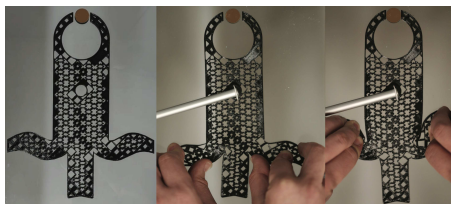


**Figure 18:** Fabricated sword gripper (black TPU). Rest shape on the left; moving handles back in the middle; moving handles to the front, holding the object, on the right.

## 4.2. 3D Examples

Our algorithm reliably handles complex geometrical models. We show a gallery of our models and some fabricated results below. Numerical results for these models are shown in Figure 19, which show a similar trend to the 2D results discussed above. For physical validation, we fabricated the gripper and bar example with TPU 88A, using the 3D printing service Xometry. As far as the authors know, no existing method can automatically and robustly produce 3D results with comparable quality: we demonstrate in Section 4.3 that simpler alternatives using solid boundary cells lead to high errors.

**Sine Bar.** The first two rows in Figure 19 show an example of a bar optimized to match a sine function when compressed. In the first row, the tiling orientation is aligned with the bar, while in the second row, we rotate the tiling to obtain similar deformation. This example shows that our method is not very sensitive to the orientation. Figure 21 shows the fabricated result of the first row, which matches closely with our simulated result.

**Gripper.** The third row in Figure 19 shows an example of a gripper, with four hands on the left and a handle on the right. We assign very stiff material to the handle (to avoid any deformation) and apply a compression force to it. The structure is optimized so that the gripper closes when the force is applied to the handle. We show a fabricated gripper in Figure 21, with force applied.

**Shoe sole.** The fourth row in Figure 19 shows an example of a box with a curved top surface. Its structure is optimized so that the deformed top surface is as flat as possible for a uniform force.

**Bird.** The last row in Figure 19 shows a bird model whose structure is optimized so that its wings go upwards as its head is pushed down.

**Batch Examples.** To further illustrate the robustness and generality of our algorithm, we show an additional gallery of 10 examples in Figure 20, computed in batch mode using a fixed objective and fixed boundary conditions. The model surface in the top 5% of the bounding box is fixed, and the surface in the bottom 5% is compressed by 10% using Dirichlet boundary conditions. The optimization maximizes the horizontal displacement under deformation integrated over the middle 10% surface. We observe that the algorithm generates intricate geometries (for reference, the size of the tetrahedral meshes used for the final simulation varies between 0.5 and 15 million tetrahedra), adapting to the complex boundaries while filling the interior with the microstructure geometry.

## 4.3. Alternative methods

We compare our method against two simple baseline approaches to handle boundary cells and the method of [TDJ\*20] (applicable only to 2D). In addition, we perform an ablation study to evaluate the effect of the second optimization (Step 4).

**Trimmed Boundary Microstructures.** A simple approach to extend two-scale microstructures to shapes with a complex boundary is trimming the parts outside the boundary shape [SBR\*15]. The downsides are obvious: arbitrarily cutting a microstructure may result in dramatic uncontrollable changes in the effective material properties, as well as entirely disconnected structures, in addition to not having a surface layer, one of the major goals of our method. We show a comparison between this method and ours in Figure 2, where it is possible to see that the method does not generally behave well – the results strongly depend on how the grid lines intersect the object. We do not use trimmed cells as a numerical baseline, as the resulting behavior depends strongly on the cell grid position with respect to the object (for our method, the dependence is not strong), so there is no single reliable number corresponding to the accuracy of this method.

**Solid Boundary Cells.** An alternative, which produces a surface layer, is filling all boundary cells with the base material, i.e. forcing the volume fraction in boundary cells to be 100% throughout the optimization. However, this adds uncontrollable stiffness to the object, especially in thinner parts, making it more restrictive than our method. On the other hand, little efficiency improvement can be gained over our method, since the number of boundary cells is much lower than interior cells. The numerical evaluation in Table 1 shows that our approach consistently outperforms this method in both reduced (i.e., using solid cells with variable material properties, as in the output of Step 2 in Section 3.4) and full (using full microstructure geometry) simulations. Additional comparisons can also be seen in Figures 2 and 3.

**Rhombic Microstructures, 2D only.** [TDJ\*20] describes a method for partitioning a mesh to cells close to the rhombic and conforming to the boundary, and constructs a suitable microstructure family. This eliminates the need for a separate cut-cell microstructure family but is hard to generalize to 3D as it requires high-quality conforming quad meshing. We compare four 2D optimization problems (disk, bar, ghost, and pliers, Figure 16) with this approach, making the best effort to replicate the problem setups, which is not entirely possible due to differences in formulation. Specifically, our objective computes an integral of the target error over the object's boundary, which is the original surface for our case, while for [TDJ\*20] it corresponds to the microstructures' interface areas for every quad in the boundary since there is no solid boundary. We observe in Figures 22 and 23 that the results are similar between the two methods. We note that [TDJ\*20] only applies to 2D, and its extension to 3D is highly non-trivial due to the requirement of a high-quality, isotropic, hexahedral mesher (see discussion in Section 2). In contrast, our method generalizes well to 3D.

**Numerical Results and an Ablation Study for the Second Optimization.** Numerical comparisons for the examples in the paper

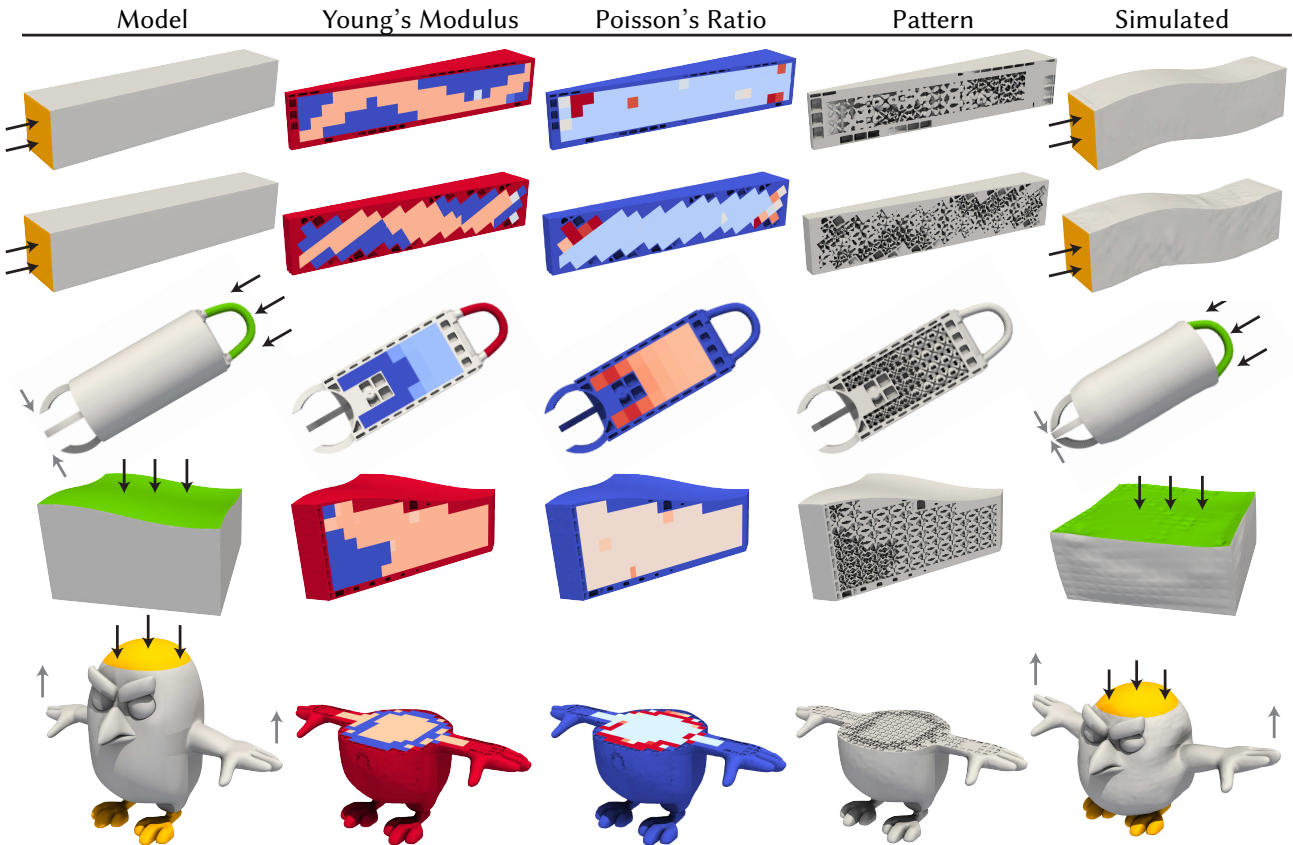


**Figure 19:** A gallery of 3D examples. From left to right: original model, optimized material distribution (Young's modulus and Poisson's ratio), final geometry at rest, and deformed geometry (simulated). In the first and last columns, surfaces with Dirichlet and Neumann boundary conditions are marked in orange and green respectively, with the displacement and force directions in black arrows. The desired deformation is marked in grey arrows.

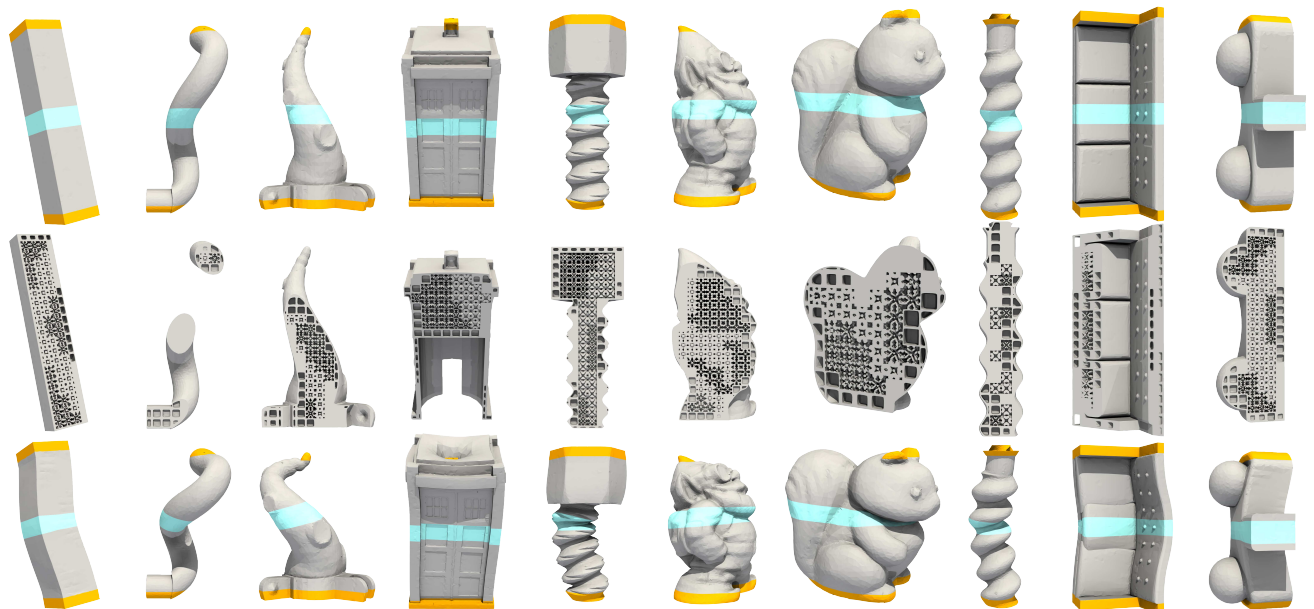


**Figure 20:** 3D examples computed in batch mode. Top: rest shape. Middle: optimized pattern. Bottom: deformed shape. The Dirichlet boundary conditions are shown in orange, the surface on which the objective is integrated is in light blue.

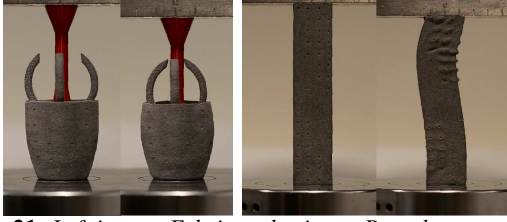


**Figure 21:** Left image: Fabricated gripper. Rest shape on the left; force applied to the handle on the right. Right image: Fabricated bar. Rest shape on the left; compressed bar deforms in a controllable way, on the right.

2D Examples	Disk	Bar	Ghost	Pliers	Bird	Sword
Solid Baseline (Full)	0.01213	0.01270	0.00792	0.00189	0.01207	0.02132
1st Opt. (Reduced)	0.00710	0.00214	0.00469	0.00009	0.00847	0.01202
2nd Opt. (Initial)	0.00834	0.00597	0.00432	0.00008	0.00718	0.01255
2nd Opt. (Reduced)	0.00826	0.00398	0.00337	0.00007	0.00670	0.01240
Our Result (Full)	0.01060	0.01057	0.00574	0.00095	0.01032	0.01841
Cells	128	356	186	287	168	209
Runtime	461	516	867	152	364	305

3D Examples	Bird	Gripper	Sine bar	Sine bar rotated	Sole
Solid Baseline (Full)	2.058	0.799	1.211	1.327	1.331
1st Opt. (Reduced)	1.540	0.232	0.550	0.452	0.010
2nd Opt. (Initial)	1.409	0.252	0.641	0.500	0.071
2nd Opt. (Reduced)	1.080	0.224	0.635	0.499	0.030
Our Result (Full)	1.620	0.030	0.586	0.437	0.259
Cells	4442	400	936	1060	1475
Runtime	20033	1738	2461	3062	3249

**Table 1:** Numerical comparisons of our approach vs. a baseline using solid boundary cells filled with base material in 2D and 3D. We report the displacement objective term in Equation 4, which represents the average point-wise error from the prescribed target for different stages of the pipeline, see Figure 5 for illustrations. The last two rows show the number of cells and runtime (sec).

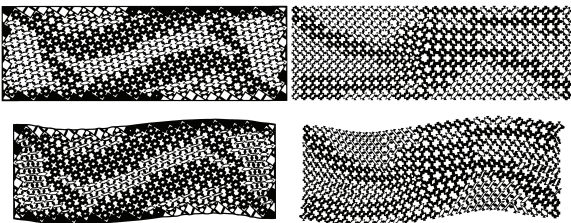


**Figure 22:** Bar example. Dirichlet conditions on both sides compress the object while targeting a sine wave shape at the top and bottom. On the left, the result obtained with our cut-cell method; on the right, the original result obtained by [TDJ\*20].

are shown in Table 1. The first optimization stage is very effective for all models (1st Opt. (Reduced) row): note however that after inserting the geometry for the boundary cells the objective might increase (2nd Opt. (Initial) row) due to the approximation of boundary cells with the reduced model. The second optimization stage (2nd Opt. (Reduced) row) significantly reduces this effect in complex cases (e.g., 2D Bar, 3D Bird, Gripper), but has a negligible effect in others (e.g. 2D Disk and Ghost). Replacing the reduced result of the second optimization with the explicit cell geometry slightly increases the objective functional again (Our Result (Full) row in the table), since the mapping  $\mathcal{P}$  in Section 3.9 assumes that both the

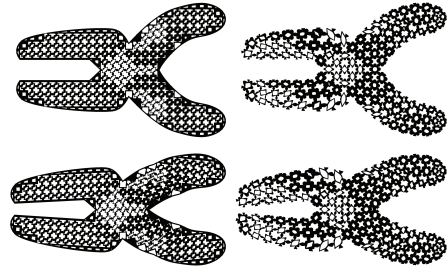


**Figure 23:** Pliers example (black TPU). We use Dirichlet conditions on the right to compress the handles with the target of closing the jaws. On the left, is the result obtained with our cutcell method; on the right, is the result of [TDJ\*20].

cell size and the deformation are infinitely small, which is not the case in practice.

Our results are consistently superior to the baseline computed with solid cells on the boundary (*Solid Baseline (Full)* row in the table).

## 5. Conclusions

We have presented a *fully automated* pipeline starting from an arbitrary 2D or 3D shape and prescribed boundary conditions, and target deformation, to a complete manufacturable geometric shape with microstructure infill, retaining the input surface, and approximating the target behavior.

**Limitations and Future Work.** Our approach has several limitations. First, for thin objects and/or relatively coarse cells, most cells would be cut cells, and the quality of the results may be lower. Some of our examples suffer from buckling of the surface layer, as no terms penalizing buckling are included in our optimization. Second, we use the linear elasticity model in our examples. Extending our work to nonlinear elasticity, including contact, would reduce the simulation-to-reality gap and could extend the applicability of our method to more complicated scenarios. However, this would require a more complex mapping between material properties and microstructure geometry. Third, replacing the optimized materials (Step 4 in Section 3.6) with geometry from the material family unavoidably introduces an error in the objective. We report statistics on this effect, shared by all two-scale optimization methods, in Table 1. We note that in simple examples where our second optimization has a minor effect on the functional, we observe that sometimes the result obtained by skipping the second optimization leads to a slightly lower functional when evaluated on the full mesh (Table 2). While unsatisfying from a theoretical point of view, these differences are negligible in practice and hard to avoid, as we cannot bound the error in the objective introduced by the use of our two-scale optimization algorithm, which is an important venue for future work.

In addition, in this work, we explored one family of structures for boundary cells. There are many possible ways to develop it further; for example, rather than keeping it entirely fixed during the second optimization stage, one can combine material optimization for interior cells with low parametric shape optimization for the

2D Examples	Disk	Bar	Ghost	Pliers	Bird	Sword
1st Opt. Full	0.01055	0.01498	0.00579	0.00094	0.01030	0.01852
2nd Opt. Full	0.01060	0.01057	0.00574	0.00095	0.01032	0.01841

3D Examples	Bird	Gripper	Sine bar	Sine bar rotated	Sole
1st Opt. Full	1.729	0.085	0.550	0.432	0.289
2nd Opt. Full	1.620	0.030	0.586	0.437	0.259

**Table 2:** Evaluation of the objective (Equation 4) on the full model with the microstructure geometry explicitly meshed after the 1st and 2nd material optimization.

boundary cells. The results can also be improved by using a broader spectrum of microstructure topologies.

## References

- [AALS17] AAGE, NIELS, ANDREASSEN, ERIK, LAZAROV, BOYAN S., and SIGMUND, OLE. “Giga-Voxel Computational Morphogenesis for Structural Design”. *Nature* 550.7674 (Oct. 2017), 84–86. DOI: 10.1038/nature23911. URL: <https://doi.org/10.1038/nature23911> 1, 3.
- [ABB\*20] ALAPPAT, CHRISTIE, BASERMANN, ACHIM, BISHOP, ALAN R., et al. “A Recursive Algebraic Coloring Technique for Hardware-Efficient Symmetric Sparse Matrix-Vector Multiplication”. *ACM Trans. Parallel Comput.* 7.3 (June 2020). ISSN: 2329-4949 8.
- [ABM98] AFTOSMIS, M. J., BERGER, M. J., and MELTON, J. E. “Robust and Efficient Cartesian Mesh Generation for Component-Based Geometry”. *AIAA Journal* 36.6 (1998), 952–960. DOI: 10.2514/2.464. eprint: <https://doi.org/10.2514/2.464>. URL: <https://doi.org/10.2514/2.464>.
- [BBO\*10] BICKEL, BERND, BÄCHER, MORITZ, OTADUY, MIGUEL A., et al. “Design and Fabrication of Materials with Desired Deformation Behavior”. *ACM Trans. Graph.* 29.4 (July 2010), 63:1–63:10. ISSN: 0730-0301. DOI: 10.1145/1778765.1778800. URL: <http://doi.acm.org/10.1145/1778765.1778800> 3.
- [Ben89] BENDSØE, MARTIN PHILIP. “Optimal shape design as a material distribution problem”. *Structural optimization* 1.4 (1989), 193–202 2.
- [BESS19] BOLLHÖFER, MATTHIAS, EFTEKHARI, ARYAN, SCHEIDEGGER, SIMON, and SCHENK, OLAF. “Large-scale Sparse Inverse Covariance Matrix Estimation”. *SIAM Journal on Scientific Computing* 41.1 (2019), A380–A401 8.
- [BRK\*22] BEAUFORT, PIERRE-ALEXANDRE, REBEROL, MAXENCE, KALMYKOV, DENIS, et al. “Hex Me If You Can”. *Computer Graphics Forum* (2022). ISSN: 1467-8659. DOI: 10.1111/cgfm.14608 3.
- [BS03] BENDSØE, MARTIN PHILIP and SIGMUND, OLE. *Topology optimization: theory, methods and applications*. Springer, 2003 2, 4.
- [BSJ\*20] BOLLHÖFER, MATTHIAS, SCHENK, OLAF, JANALIK, RADIM, et al. “State-of-the-Art Sparse Direct Solvers”. (2020). Ed. by GRAMA, ANANTH and SAMEH, AHMED H., 3–33 8.
- [Car23] CARBON3D. *Carbon Design Engine*. Carbon Design Engine. 2023. URL: <https://www.carbon3d.com/products/carbon-design-engine> 1.
- [CD99] CIORANESCU, DOINA and DONATO, PATRIZIA. *An introduction to homogenization*. Oxford University Press, 1999 2.
- [DBHG21] DJOURACHKOVITCH, TRISTAN, BLAL, NAWFAL, HAMILA, NAHIENE, and GRAVOUIL, ANTHONY. “Multiscale topology optimization of 3D structures: A micro-architected materials database assisted strategy”. *Computers & Structures* 255 (2021), 106574 3.
- [GJ\*10] GUENNEBAUD, GAËL, JACOB, BENOÎT, et al. *Eigen v3*. <http://eigen.tuxfamily.org>. 2010 8.
- [GPZ19] GIL-URETA, FRANCISCA, PIETRONI, NICO, and ZORIN, DENIS. “Structurally Optimized Shells”. *arXiv preprint arXiv:1904.12240* (2019) 3.
- [GS17] GROEN, JEROEN P. and SIGMUND, OLE. “Homogenization-Based Topology Optimization for High-Resolution Manufacturable Microstructures”. *International Journal for Numerical Methods in Engineering* 113.8 (Aug. 2017), 1148–1163. DOI: 10.1002/nme.5575. URL: <https://doi.org/10.1002/nme.5575> 3.
- [GWS19] GROEN, JEROEN P., WU, JUN, and SIGMUND, OLE. “Homogenization-Based Stiffness Optimization and Projection of 2D Coated Structures With Orthotropic Infill”. *Computer Methods in Applied Mechanics and Engineering* 349 (June 2019), 722–742. DOI: 10.1016/j.cma.2019.02.031. URL: <https://doi.org/10.1016/j.cma.2019.02.031> 3.
- [HK22] HACHENBERGER, PETER and KETTNER, LUTZ. “3D Boolean Operations on Nef Polyhedra”. *CGAL User and Reference Manual*. 5.5.1. CGAL Editorial Board, 2022. URL: <https://doc.cgal.org/5.5.1/Manual/packages.html#pkgNef3> 4.
- [HSW\*20] HU, YIXIN, SCHNEIDER, TESEO, WANG, BOLUN, et al. “Fast tetrahedral meshing in the wild”. *ACM Transactions on Graphics (TOG)* 39.4 (2020), 117–1 5, 8.
- [HTG\*22] HUANG, ZIZHOU, TOZONI, DAVI COLLI, GJOKA, ARVI, et al. *Differentiable solver for time-dependent deformation problems with contact*. 2025. arXiv: 2205.13643 [cs.GR] 5.
- [JKS13] JACOBSON, ALEC, KAVAN, LADISLAV, and SORKINE-HORNUNG, OLGA. “Robust Inside-Outside Segmentation Using Generalized Winding Numbers”. *ACM Trans. Graph.* 32.4 (July 2013). ISSN: 0730-0301. DOI: 10.1145/2461912.2461916. URL: <https://doi.org/10.1145/2461912.2461916> 5.
- [KMvHW19] KADIC, MUAMER, MILTON, GRAEME W., van HECKE, MARTIN, and WEGENER, MARTIN. “3D metamaterials”. *Nature Reviews Physics* 1.3 (2019), 198–210 2.
- [KPCP18] KONAKOVIĆ-LUKOVIĆ, MINA, PANETTA, JULIAN, CRANE, KEENAN, and PAULY, MARK. “Rapid deployment of curved surfaces via programmable auxetics”. *ACM Transactions on Graphics (TOG)* 37.4 (2018), 106 3.
- [LB23] LIU, HENG and BOMMES, DAVID. “Locally Meshable Frame Fields”. *ACM Trans. Graph.* 42.4 (2023) 2.
- [LHZ\*18] LIU, HAIXIANG, HU, YUANMING, ZHU, BO, et al. “Narrow-Band Topology Optimization on a Sparsely Populated Grid”. *ACM Trans. Graph.* 37.6 (Dec. 2018), 251:1–251:14. ISSN: 0730-0301. DOI: 10.1145/3272127.3275012. URL: <http://doi.acm.org/10.1145/3272127.3275012> 3.
- [LLWW18] LIU, YANG, LI, ZUYU, WEI, PENG, and WANG, WENWEN. “Parameterized level-set based topology optimization method considering symmetry and pattern repetition constraints”. *Computer Methods in Applied Mechanics and Engineering* 340 (2018), 1079–1101 3.
- [MBH17] MILTON, GRAEME W., BRIANE, MARK, and HARUTYUNYAN, DAVIT. “On the possible effective elasticity tensors of 2-dimensional and 3-dimensional printed materials”. *Mathematics and Mechanics of Complex Systems* 5.1 (2017), 381–391 3.
- [MDL16] MARTÍNEZ, JONÁS, DUMAS, JÉRÉMIE, and LEFEBVRE, SYLVAIN. “Procedural Voronoi foams for additive manufacturing”. *ACM Transactions on Graphics (TOG)* 35.4 (2016), 44 3.
- [Mil02] MILTON, GRAEME W. *The theory of composites*. Cambridge University Press, 2002 2.
- [MPI\*18] MALOMO, LUIGI, PÉREZ, JESÚS, IARUSSI, EMMANUEL, et al. “FlexMaps: Computational Design of Flat Flexible Shells for Shaping 3D Objects”. *ACM Trans. Graph.* 37.6 (Dec. 2018), 241:1–241:14. ISSN: 0730-0301. DOI: 10.1145/3272127.3275076. URL: <http://doi.acm.org/10.1145/3272127.3275076> 3.
- [MSDL17] MARTÍNEZ, JONÁS, SONG, HAICHUAN, DUMAS, JÉRÉMIE, and LEFEBVRE, SYLVAIN. “Orthotropic K-Nearest Foams for Additive Manufacturing”. *ACM Transactions on Graphics* 36.4 (July 2017), 1–12. DOI: 10.1145/3072959.3073638 3.

- [Mus13] MUSETH, KEN. “VDB: High-Resolution Sparse Volumes with Dynamic Topology”. *ACM Trans. Graph.* 32.3 (July 2013). ISSN: 0730-0301. DOI: 10.1145/2487228.2487235. URL: <https://doi.org/10.1145/2487228.2487235>.
- [nTo23] NTOPOLOGY. *nTop Platform*. Engineering software built for digital manufacturing. 2023. URL: <https://ntopology.com/> 1, 2.
- [PCS\*22] PIETRONI, NICO, CAMPEN, MARCEL, SHEFFER, ALLA, et al. “Hex-Mesh Generation and Processing: A Survey”. *ACM Trans. Graph.* 42.2 (Oct. 2022). ISSN: 0730-0301. DOI: 10.1145/3554920. URL: <https://doi.org/10.1145/3554920>.
- [PP19] PLOCHER, JÁNOS and PANESAR, AJIT. “Review on design and structural optimisation in additive manufacturing: Towards next-generation lightweight structures”. *Materials & Design* 183 (2019), 108164 3.
- [PRZ17] PANETTA, JULIAN, RAHIMIAN, ABTIN, and ZORIN, DENIS. “Worst-Case Stress Relief for Microstructures”. *ACM Transactions on Graphics* 36.4 (July 2017), 1–16. DOI: 10.1145/3072959.3073649 8.
- [PZM\*15] PANETTA, JULIAN, ZHOU, QINGNAN, MALOMO, LUIGI, et al. “Elastic textures for additive fabrication”. *ACM Transactions on Graphics (TOG)* 34.4 (2015), 135 2–4, 7, 8.
- [RWH22] RASTEGARZADEH, SINA, WANG, JUN, and HUANG, JIDA. “Two-Scale Topology Optimization with Isotropic and Orthotropic Microstructures”. *Designs* 6.5 (2022), 73 3.
- [SBR\*15] SCHUMACHER, CHRISTIAN, BICKEL, BERND, RYS, JAN, et al. “Microstructures to control elasticity in 3D printing”. *ACM Transactions on Graphics (TOG)* 34.4 (2015), 136 2, 3, 10.
- [SDG\*19] SCHNEIDER, TESEO, DUMAS, JÉRÉMIE, GAO, XIFENG, et al. *PolyFEM*. <https://polyfem.github.io/>. 2019 5, 8.
- [She05] SHEWCHUK, JONATHAN RICHARD. “Triangle: Engineering a 2D quality mesh generator and Delaunay triangulator”. *Applied Computational Geometry Towards Geometric Engineering: FCRC’96 Workshop, WACG’96 Philadelphia, PA, May 27–28, 1996 Selected Papers*. Springer. 2005, 203–222 8.
- [She96] SHEWCHUK, JONATHAN RICHARD. “Triangle: Engineering a 2D quality mesh generator and Delaunay triangulator”. *Workshop on Applied Computational Geometry*. Springer. 1996, 203–222 7.
- [SPP21] SANDERS, ED, PEREIRA, A, and PAULINO, GH. “Optimal and continuous multilattice embedding”. *Science Advances* 7.16 (2021), eabf4838 3.
- [STC\*13] SKOURAS, MÉLINA, THOMASZEWSKI, BERNHARD, COROS, STELIAN, et al. “Computational design of actuated deformable characters”. *ACM Transactions on Graphics (TOG)* 32.4 (2013), 82 3.
- [TBFL19] TAO, MICHAEL, BATTY, CHRISTOPHER, FIUME, EUGENE, and LEVIN, DAVID. “Mandoline: Robust Cut-Cell Generation for Arbitrary Triangle Meshes”. *ACM Transactions on Graphics* (2019) 4.
- [TDJ\*20] TOZONI, DAVI COLLI, DUMAS, JÉRÉMIE, JIANG, ZHONGSHI, et al. “A low-parametric rhombic microstructure family for irregular lattices”. *ACM Transactions on Graphics (TOG)* 39.4 (2020), 101–1 2–4, 7, 8, 10, 12.
- [Tor02] TORQUATO, SALVATORE. *Random heterogeneous materials: microstructure and macroscopic properties*. Vol. 16. Springer, 2002 2.
- [WAWS18] WU, JUN, AAGE, NIELS, WESTERMANN, RUDIGER, and SIGMUND, OLE. “Infill Optimization for Additive Manufacturing—Approaching Bone-Like Porous Structures”. *IEEE Transactions on Visualization and Computer Graphics* 24.2 (Feb. 2018), 1127–1140. DOI: 10.1109/tvcg.2017.2655523. URL: <https://doi.org/10.1109/tvcg.2017.2655523>.
- [WCOR21] WANG, JUN, CALLANAN, JESSE, OGUNBODEDE, OLADAPO, and RAI, RAHUL. “Hierarchical combinatorial design and optimization of non-periodic metamaterial structures”. *Additive Manufacturing* 37 (2021), 101710 3.
- [WDW16] WU, JUN, DICK, CHRISTIAN, and WESTERMANN, RUDIGER. “A System for High-Resolution Topology Optimization”. *IEEE Transactions on Visualization and Computer Graphics* 22.3 (Mar. 2016), 1195–1208. DOI: 10.1109/tvcg.2015.2502588. URL: <https://doi.org/10.1109/tvcg.2015.2502588>.
- [WSG21] WU, JUN, SIGMUND, OLE, and GROEN, JEROEN P. “Topology optimization of multi-scale structures: a review”. *Structural and Multidisciplinary Optimization* 63.3 (2021), 1455–1480 3.
- [XB15] XIA, LIANG and BREITKOPF, PIOTR. “Multiscale structural topology optimization with an approximate constitutive model for local material microstructure”. *Computer Methods in Applied Mechanics and Engineering* 286 (2015), 147–167 3.
- [ZSCM17] ZHU, BO, SKOURAS, MÉLINA, CHEN, DESAI, and MATUSIK, WOJCIECH. “Two-Scale Topology Optimization With Microstructures”. *ACM Trans. Graph.* 36.4 (July 2017). ISSN: 0730-0301. DOI: 10.1145/3072959.3095815. URL: <http://doi.acm.org/10.1145/3072959.3095815>.